Very strong interaction between FeN$_4$ and titanium carbide for durable

4-electron oxygen reduction reaction suppressing catalyst deactivation

by peroxide

Yeongdae Lee,‡[a] Jang Hyuk Ahn,‡[a] Haeseong Jang,‡[b] Jisu Lee,[a] Subhin Yoon,[a] Dong-Gyu Lee,[a] Min Gyu Kim,*[b] Jun Hee Lee,*[a] Hyun-Kon Song*[a]
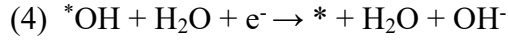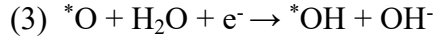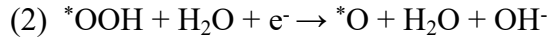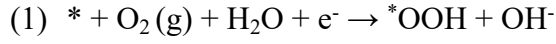
Computational Details

The Vienna ab initio simulation package (VASP)[1–4] with projector augmented wave (PAW) pseudopotentials was used for density functional theory (DFT) calculation.[5,6] For the exchange-correlation energy, the Perdew-Burke-Ernzerhof (PBE)[7] and the PBE functional with van der Waals interaction of the Grimme's method PBE-D2[8] using the default parameter was utilized with a plane-wave cutoff of 500 eV. All calculations were spin-polarized and Gaussian smearing method with the 1.0E-6 eV energy criteria was applied for electronic self-consistent loop. Atomic positions were relaxed until interatomic force on uninhibited atoms were smaller than 0.02 eV/Å. The crystal orbital Hamilton populations (COHPs) were calculated to investigate the bond orbital interaction between metal and oxygen species.[9–13]

Minimum 15 Å-thick vacuum was introduced to the FePc and FePc/1L-Ti_3C_2 slabs along the z-direction to reduce the periodic image interference. The single FePc molecule was constructed to have its square-planar plane on the xy-plane. The FePc slab was 18.5 Å ✕ 18.5 Å ✕ 29.2 Å (**Fig. S6a**). The slab of FePc supported by 1L-Ti_3C_2 (FePc/1L-Ti_3C_2) was constructed by placing the single FePc molecule along the z-direction on the 1L-Ti_3C_2 support supercell slab having 108 titanium and 72 carbon atoms in 18.6 Å ✕ 18.6 Å ✕ 29.3 Å (**Fig. S6b**). The Brillouin zone was integrated with 2 ✕ 2 ✕ 1 Gamma grid k-point mesh. The FePc/1L-Ti_3C_2 slab was thermodynamically most stable when a single Fe atom of FePc was coordinated two Ti atoms of 1L-Ti_3C_2 (double coordination via $FeTi_2$ in **Fig. S7**).

The ORR proceeded on the Fe atom of both supported and unsupported FePc. On the four-electron (4e) ORR process in alkaline media, molecular oxygen is reduced to hydroxide ions via:[14–16]

$$O_2 + 2H_2O + 4e^- \rightarrow 4OH^- \qquad E^\circ = 1.23 \text{ V } vs. \text{ RHE}$$

Four reaction steps were considered for drawing free energy diagrams in alkaline media:

(1) $* + O_2\,(g) + H_2O + e^- \rightarrow {}^*OOH + OH^-$

(2) ${}^*OOH + H_2O + e^- \rightarrow {}^*O + H_2O + OH^-$

(3) ${}^*O + H_2O + e^- \rightarrow {}^*OH + OH^-$

(4) ${}^*OH + H_2O + e^- \rightarrow * + H_2O + OH^-$

where the asterisk mark (*) indicates an adsorbed species on the Fe active site.

Free energies (ΔG) or binding energies of the ORR intermediate adsorbate to active sites were calculated with respect to RHE by:

$\Delta G = \Delta E + \Delta ZPE - T\Delta S - qU + k_BT \ln(10)\text{\textxi}\,pH$

where ΔE = the total energy change; ΔZPE = zero point energy; $T\Delta S$ = entropic energy; q = charge transfer for each reaction step; U = the applied potential; k_B = Boltzmann constant. The ZPEs were calculated by frozen phonon method.

Bader charges (ΔQ) of Fe of FePc as well as ORR intermediates were calculated along the 4e ORR pathway. The ΔQ values of Fe and the intermediates were estimated with respect to Fe atom and molecular oxygen (O_2).
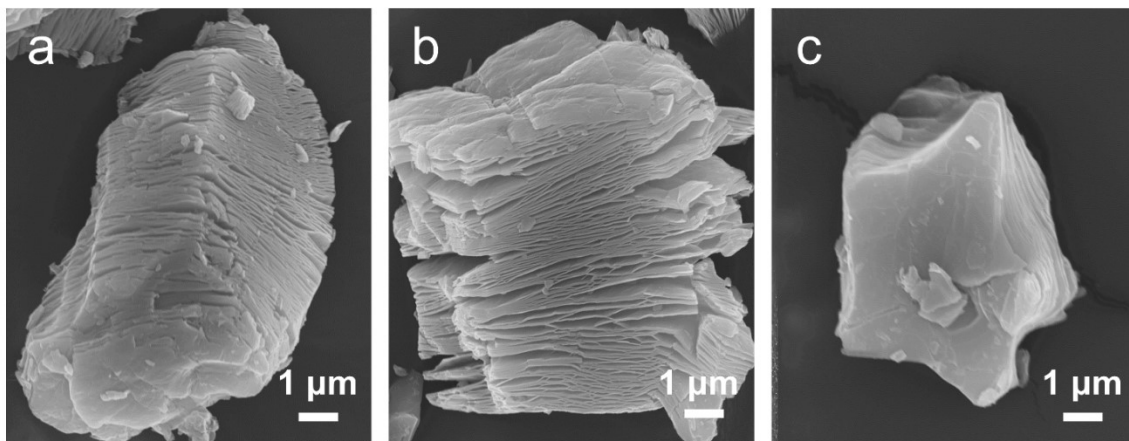
Fig. S1. Bulky Ti$_3$C$_2$ having multiple layers (mL-Ti$_3$C$_2$) in SEM images. (**a**) Overall view. (**b**) Edge view. (**c**) Basal view.
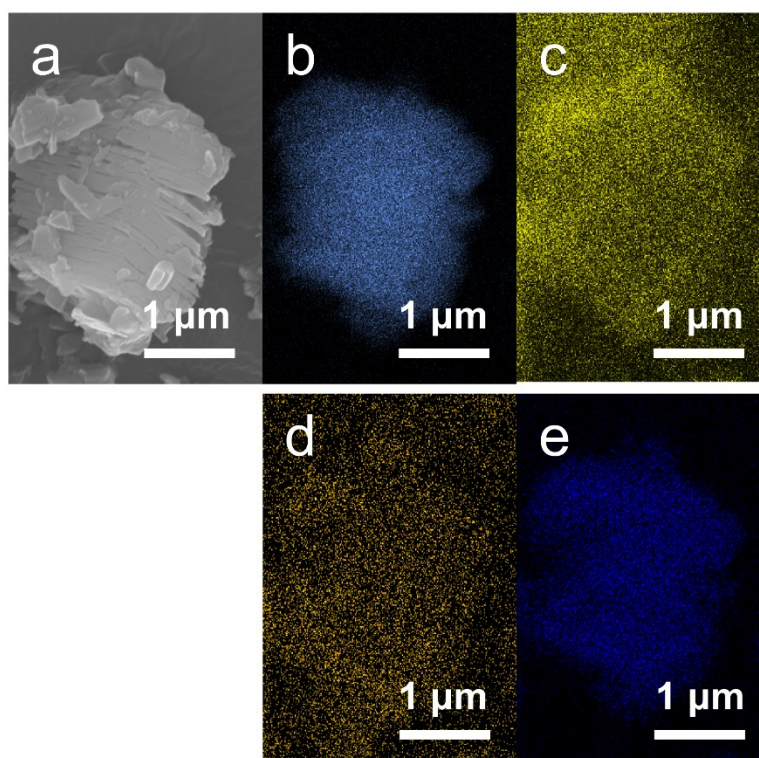

Fig. S2. Edge plane of FePc/mL-Ti$_3$C$_2$ in elemental maps by energy-dispersive X-ray spectroscopy (EDS). (**a**) Scanning-electron-microscopic (SEM) image. (**b**) Ti. (**c**) C. (**d**) Fe. (**e**) N.
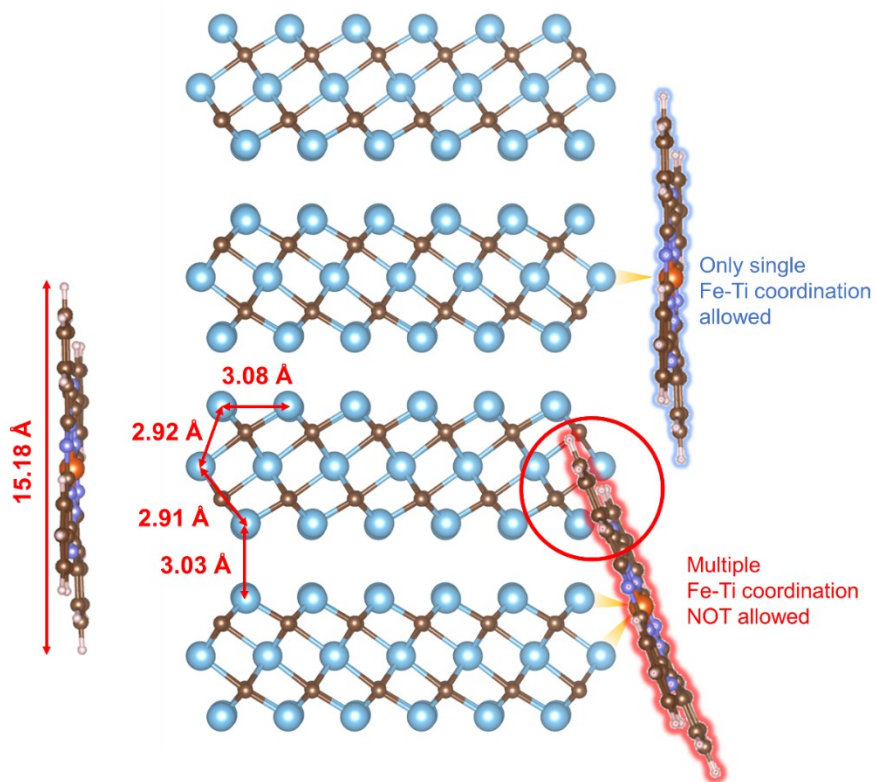
Fig. S3. Adsorption of FePc onto edge planes of bulky Ti$_3$C$_2$ having multilayers. The right side of this schematic picture demonstrates that only single Fe-Ti coordination between FePc and Ti$_3$C$_2$ is allowed when FePc is adsorbed on the edge plane of Ti$_3$C$_2$.
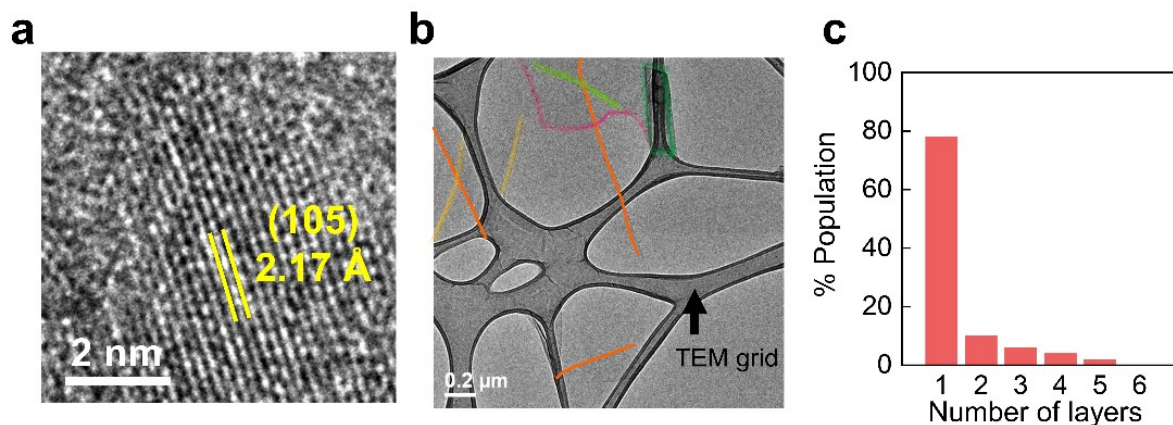
Fig. S4. Two-dimensional Ti₃C₂ monolayer leaf (1L-Ti₃C₂). (**a**) Basal plane by TEM. (**b**) Several overlapped monolayer leaves by TEM. The boundary of 1L-Ti$_3$C$_2$ leaves was sketched for clarity, each color indicating a separate leaf. (**c**) Population distribution of the number of layers.
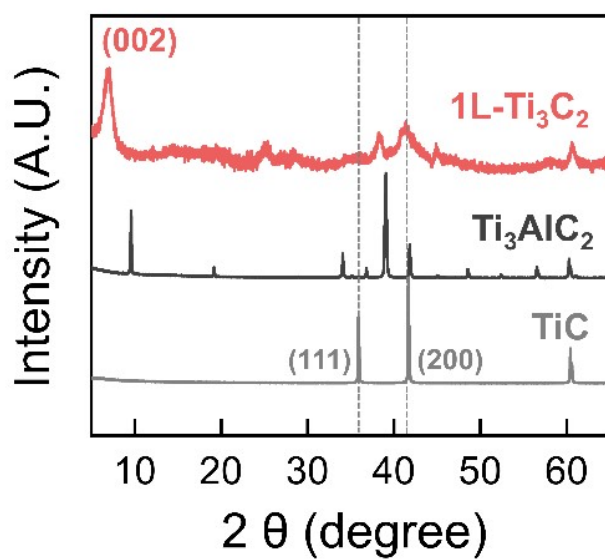

Fig. S5. XRD spectra of 1L-Ti₃C₂, Ti₃AlC₂ and TiC.

Negligible ORR currents on 1L-Ti₃C₂ as the support without FePc as the ORR catalyst.
A large overpotential was required for ORR on 1L-Ti$_3$C$_2$ in the absence of FePc (**Fig. S6a**).
The onset potential of ORR on 1L-Ti$_3$C$_2$ was 0.8 V$_{RHE}$, 0.2 V more negative than that of
FePc/1L-Ti$_3$C$_2$. The ORR current of 1L-Ti$_3$C$_2$ was negligible at > 0.8 V$_{RHE}$ where the current
of FePc/1L-Ti$_3$C$_2$ increased exponentially. Therefore, we concluded that the catalytic ORR
currents were dominantly driven by FePc, not its supports, before reaching their limiting value
(i_l = -5.6 mA cm^{-2}).

Another lesson we can learn from the ORR polarization curves (**Fig. S6a**) is that 4-
electron (4e) ORR was more favored on FePc supported by 1L-Ti$_3$C$_2$ while the support without
catalysts significantly produced peroxide (HO$_2^-$) as an incompletely reduced species via 2e
ORR. The number of electrons transferred (n) of the ORR on FePc/1L-Ti$_3$C$_2$ was estimated to
be almost 4, which was read from its i_l by Levich equation. On the other hand, the i_l of 1L-
Ti$_3$C$_2$ without catalysts was around a half of FePc/1L-Ti$_3$C$_2$, supporting 2e ORR rather than 4e
ORR. At cathodic potentials enough to encourage both the ORR currents on FePc-present and
FePc-absent 1L-Ti$_3$C$_2$ to reach their limiting values, n was calculated from disk and ring
currents of rotating ring disk electrode experiments: n = ~4 for FePc/1L-Ti$_3$C$_2$; n = ~3 for 1L-
Ti$_3$C$_2$. 1L-Ti$_3$C$_2$ was not able to reduce oxygen molecules completely even at enough
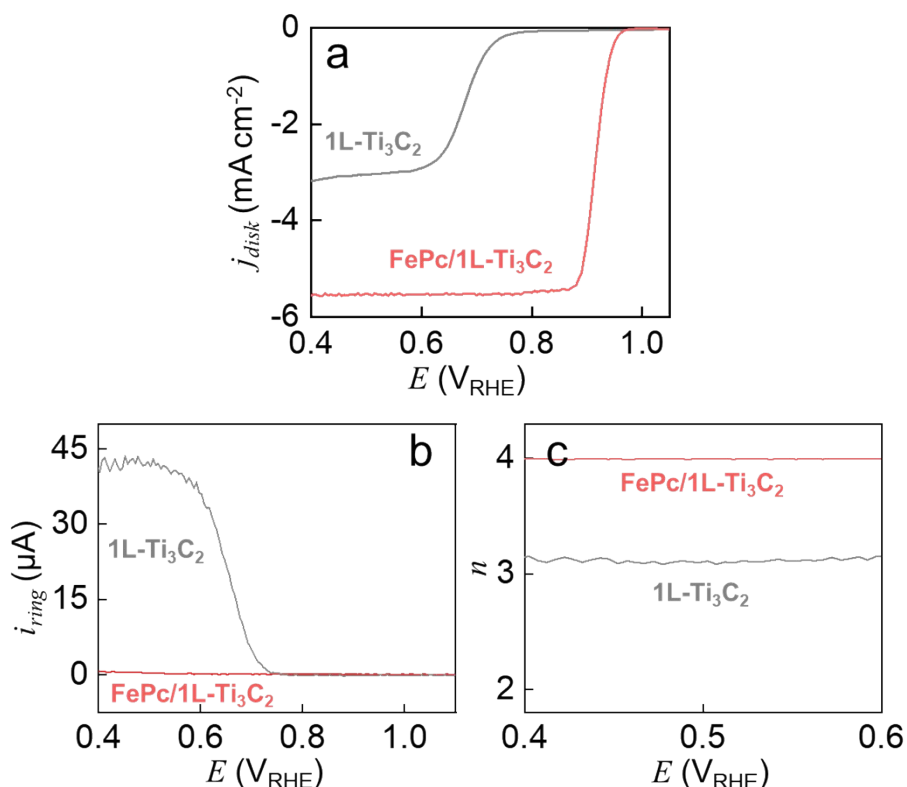overpotentials.

Fig. S6. ORR on 1L-Ti₃C₂ with and without FePc. Disk potential was cathodically scanned
The disk electrode was rotated at 1600 rpm in 0.1 M KOH (aq). (**a**) Disk current density (j_{disk})
along disk potential. (**b**) Ring current (i_{ring}) along disk potential. (**c**) The number of electron
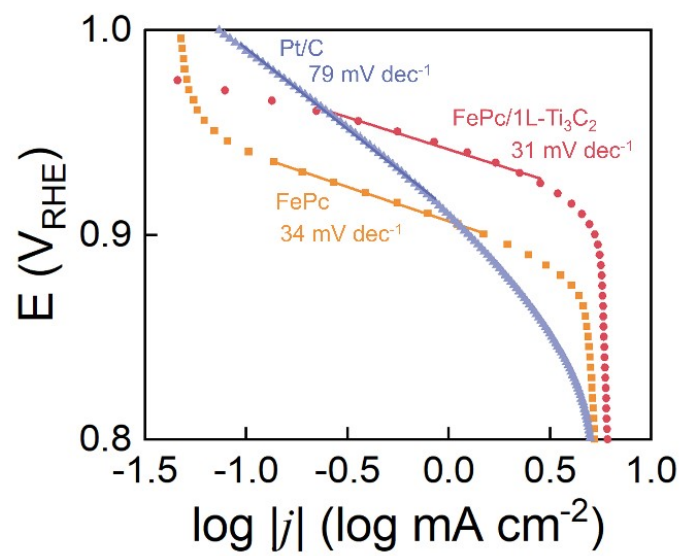transferred (n) calculated from disk and ring currents.

Fig. S7. Tafel plots.

Table S1. ORR metrics comparison of electrocatalysts based on FeN$_4$ and Fe-N-C active sites. E_{onset} = onset potential; $E_{1/2}$ = half-wave potential; b = Tafel slope.

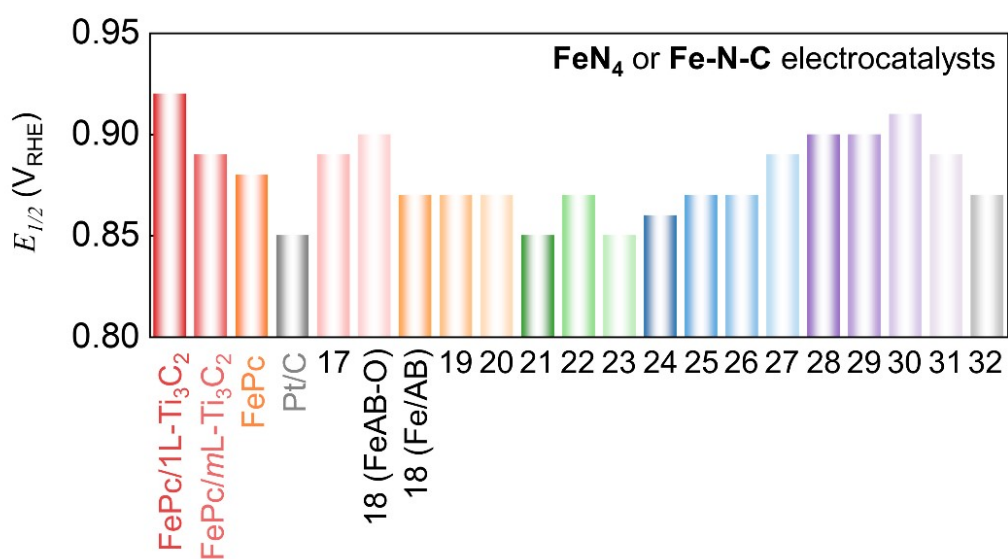| Electrocatalysts	E_{onset} V$_{RHE}$	$E_{1/2}$ V$_{RHE}$	b mV dec^{-1}	Reference
FePc/1L-Ti$_3$C$_2$	1.00	0.92	31	This work
FePc/mL-Ti$_3$C$_2$	0.97	0.89	-	This work
FePc	0.96	0.88	34	This work
Pt/C	1.03	0.85	79	This work
FePc/mL-Ti$_3$C$_2$	0.97	0.89	-	17
FeAB-O	0.98	0.90	27.5	18
FePc/AB	0.96	0.87	37.5	18
Fe-SAs/NSC	1.00	0.87	-	19
Fe-N/P-C-700	0.94	0.87	-	20
Fe/OES	1.00	0.85	-	21
PCNT@Fe@GL	0.97	0.87	61.9	22
Fe/SNC	0.97	0.85	-	23
FePhen@MOFArNH$_3$	1.03	0.86	-	24
Fe$_2$-Z$_8$-C	0.98	0.87	-	25
FeSAs/PTF-600	1.01	0.87	-	26
SA-Fe-HPC	1.00	0.89	49	27
Fe-ISA/NC	-	0.90	-	28
Fe-ISAs/CN	0.99	0.90	-	29
Fe SAs-N/C-20	-	0.91	-	30
Fe$_{SA}$-N-C	-	0.89	-	31
SA-Fe/NHPC	-	0.87	-	32

Fig. S8. $E_{1/2}$ comparison from Table S1.
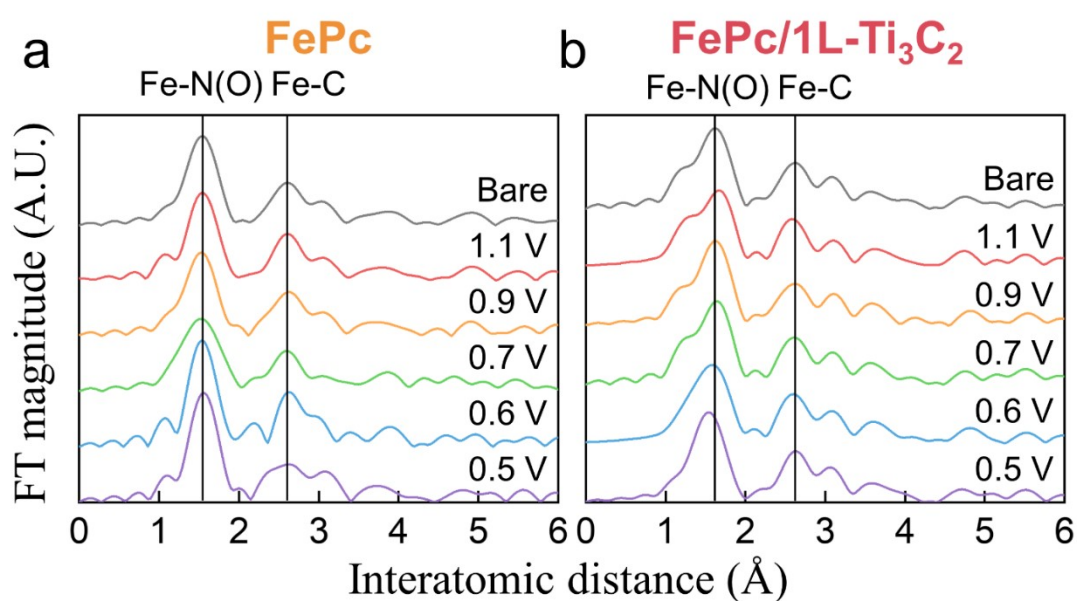
Fig. S9. Radial distribution functions obtained by Fourier-transforming EXAFS spectra at indicated potentials. (**a**) FePc. (**b**) FePc/1L-Ti$_3$C$_2$.
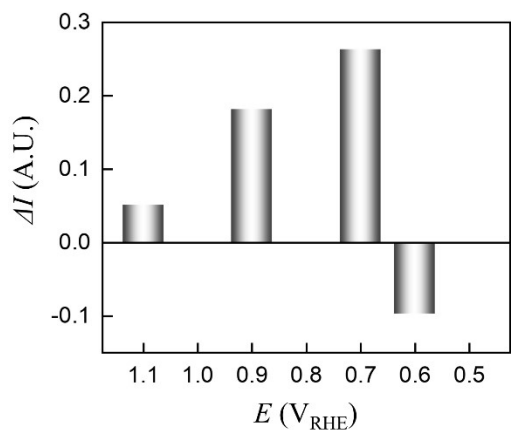
Fig. S10. The difference of the maximum intensities between FePc/1L-Ti$_3$C$_2$ and FePc at indicated potentials. $\Delta I = I_{\text{FePc/1L-Ti3C2}} - I_{\text{FePc}}$ with I = maximum intensity. The values of I was read around 1.5 Å from **Fig. 2b**.
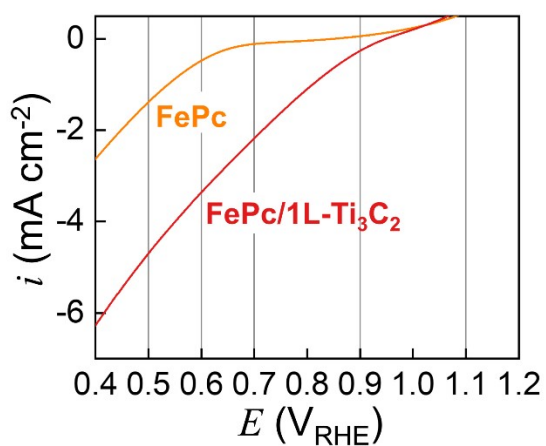

Fig. S11. Electrochemical responses of ORR in the cells used for the *Operando* EXAFS experiments (Fig. 2b). The cells were constructed with three electrodes: catalyst-loaded carbon papers as the working electrode; platinum as the counter electrode; and Hg/HgO as the reference electrode.
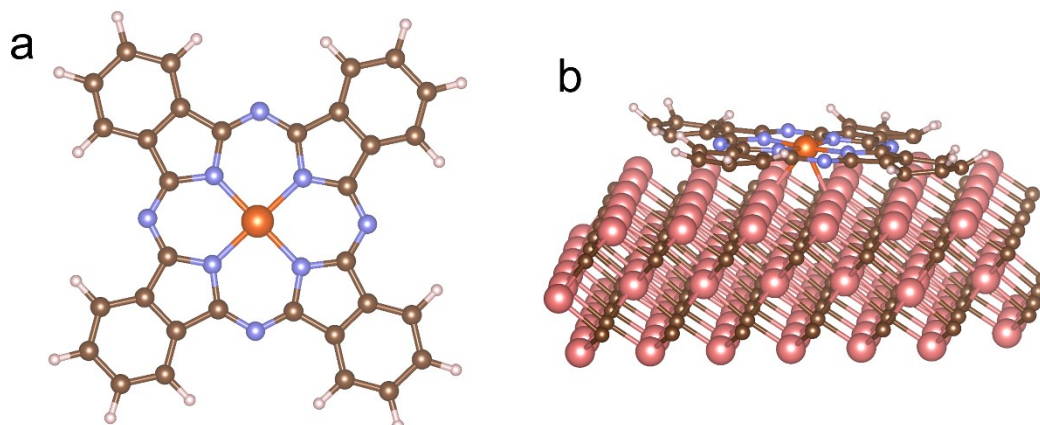
Fig. S12. Structures. Refer to **Fig. 1a** for the atomic colors. (**a**) FePc. (**b**) FePc/1L-Ti$_3$C$_2$ with FeTi$_2$ coordination.
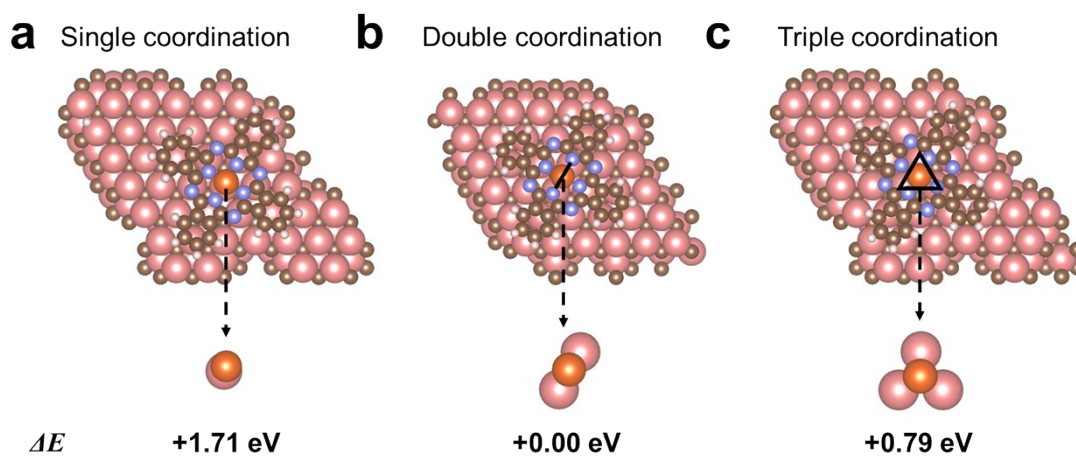

Fig. S13. The coordination between Fe of FePc and Ti of 1L-Ti$_3$C$_2$. Refer to **Fig. 1a** for the atomic colors. The binding energies of FePc to 1L-Ti$_3$C$_2$ (*ΔE*) were indicated with respect to the double coordination in **b**. (**a**) FeTi coordination. (**b**) FeTi$_2$ coordination. (**a**) FeTi$_3$ coordination.
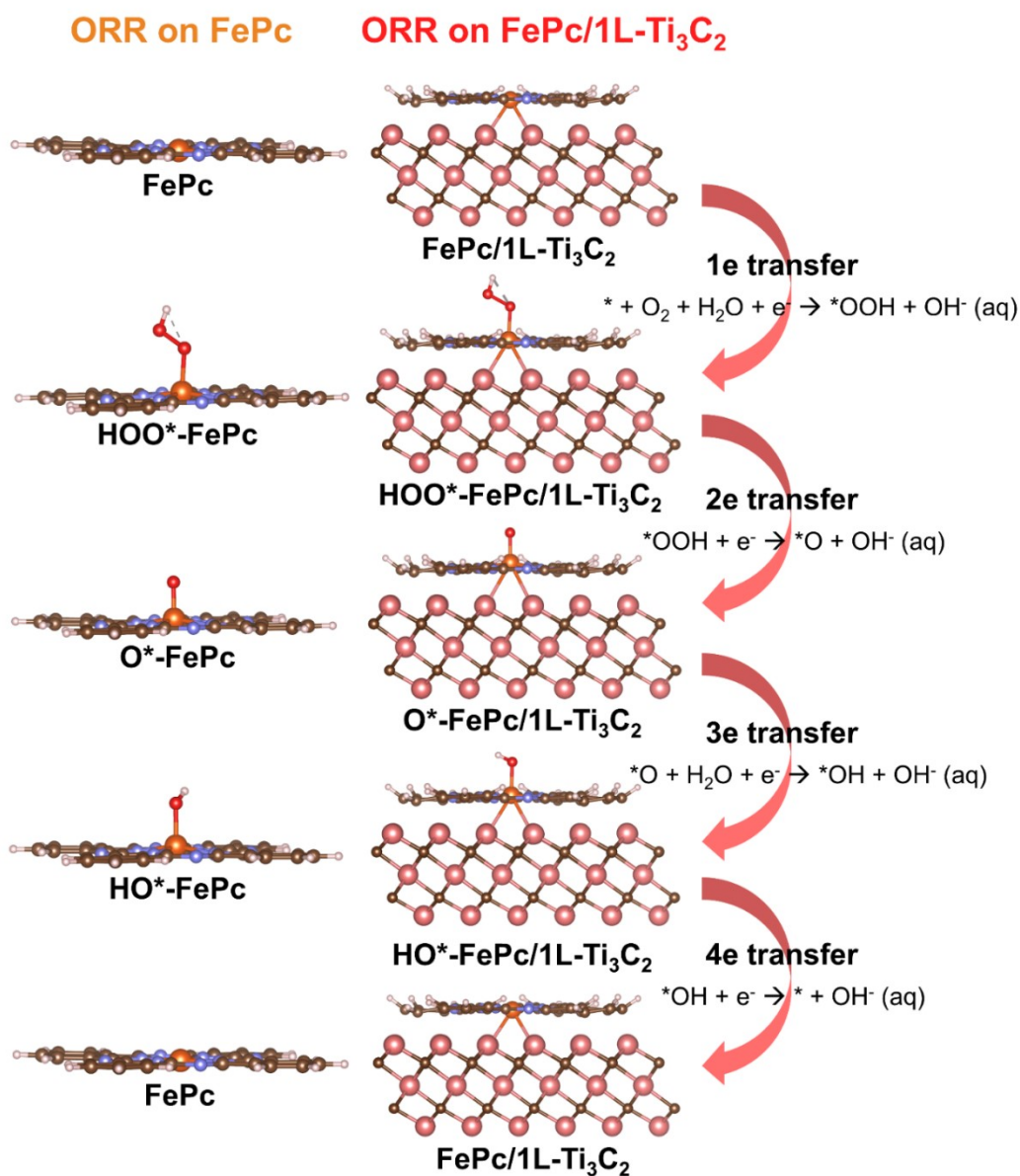
Fig. S14. Four-electron (4e) ORR pathway on FePc and FePc/1L-Ti₃C₂. The molecular configurations were calculated by DFT.
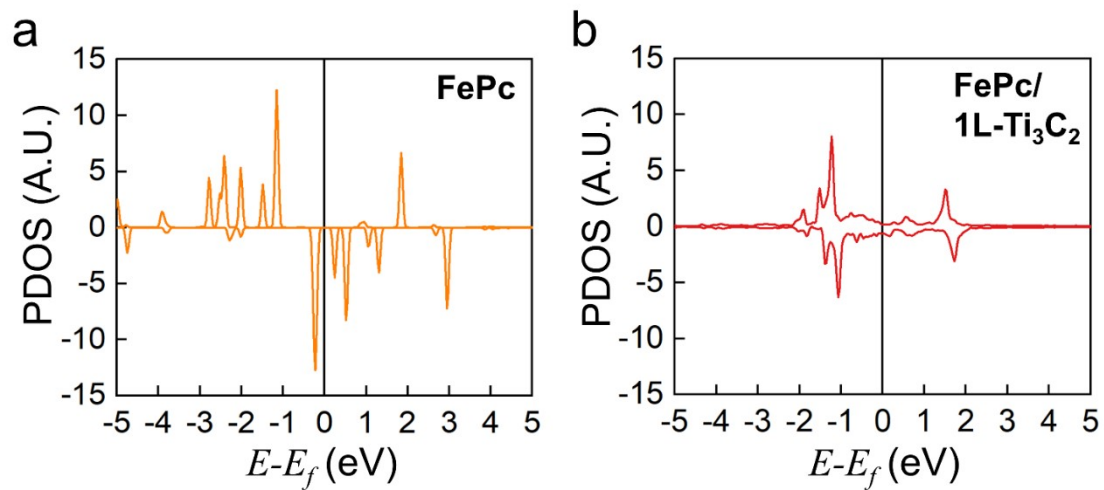
Fig. S15. Projected density of states (PDOS) of Fe d-orbital. E = energy; E_f = Fermi level.
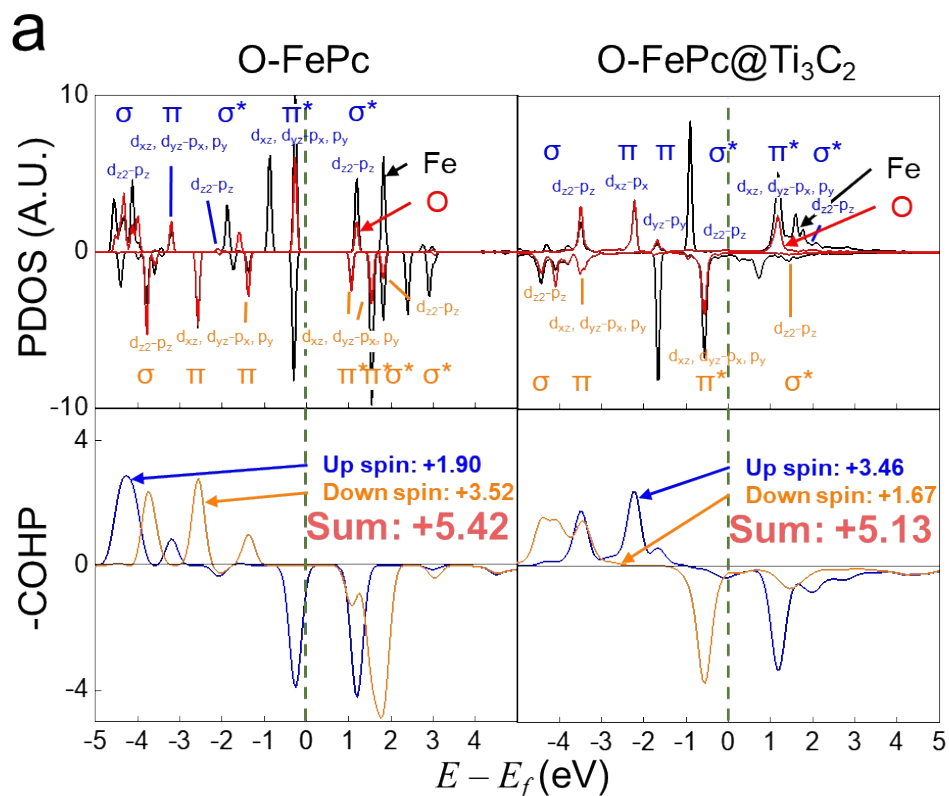
(**a**) FePc. (**b**) FePc/1L-Ti$_3$C$_2$.

Fig. S16. Partial density of states (PDOS) and crystal orbital Hamiltonian population (-*COHP*) of the ORR intermediates adsorbed on 1L-Ti$_3$C$_2$-supported and unsupported FePc. E = energy; E_f = Fermi level; σ and σ* = bonding and antibonding sigma molecular orbitals, respectively (resulting from the combination of Fe d$_z^2$ and O p$_z$); π and π* = bonding and antibonding pi molecular orbitals, respectively (Fe d$_{yz}$, d$_{zx}$ and O p$_x$, p$_y$). The net summation of -COHP was indicated as a measure of bonding strength. **(a)** *O. **(b)** *OH. **(c)** *OOH.
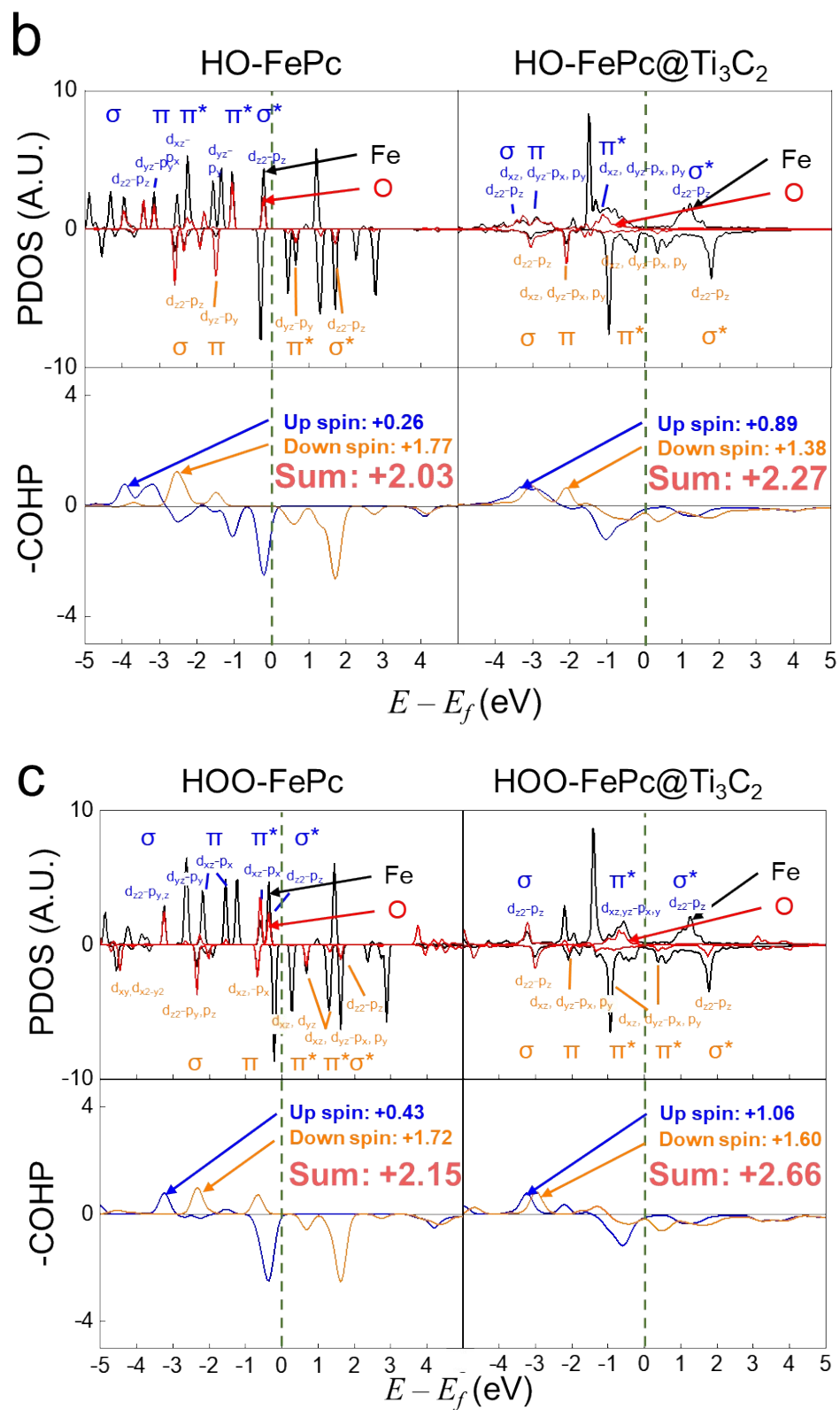
Fig. S16. (Continued) **PDOS and -*COHP*.**
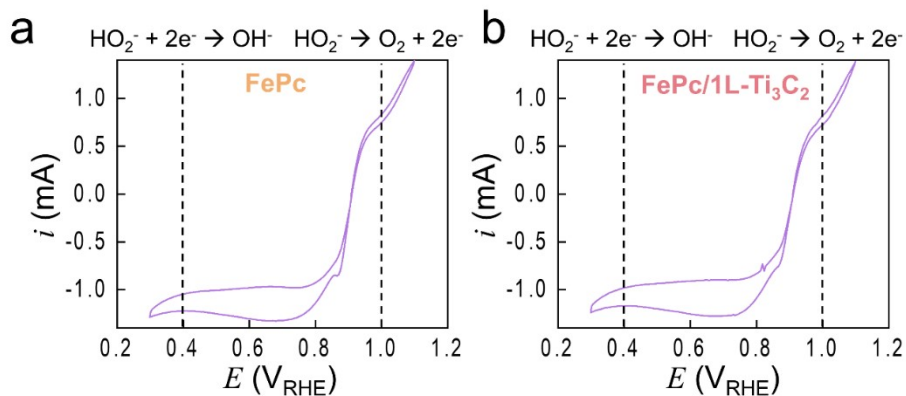
Fig. S17. Cyclic voltammograms of peroxide reduction reaction (PRR) at the cathodic scan and peroxide oxidation reaction (POR) at the anodic scan. Counter electrode = Graphite rod; Reference electrode = Hg/HgO; Electrolyte = Ar-purged 0.1 M KOH with 10 mM peroxide; 1600 rpm with 50 mV s^{-1}. (**a**) FePc. (**b**) FePc/1L-Ti$_3$C$_2$.

Fig. S18. Free energy (ΔG) diagrams along the 2-electron-transfer (2e) ORR pathway at the standard reduction potential of peroxide generation (0.7 V$_{RHE}$).

References

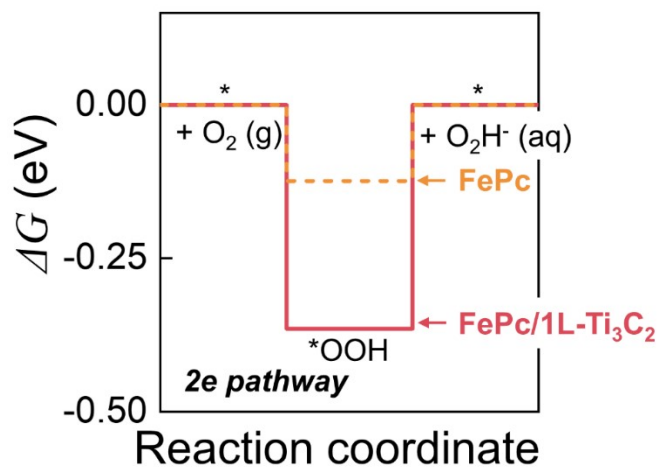1   G. Kresse and J. Furthmüller, *Phys. Rev. B*, 1996, **54**, 11169–11186.

2   G. Kresse and J. Furthmüller, *Comput. Mater. Sci.*, 1996, **6**, 15–50.

3   G. Kresse and J. Hafner, *Phys. Rev. B*, 1994, **49**, 14251–14269.

4   G. Kresse and J. Hafner, *Phys. Rev. B*, 1993, **47**, 558–561.

5   G. Kresse and D. Joubert, *Phys. Rev. B*, 1999, **59**, 1758–1775.

6   P. E. Blöchl, *Phys. Rev. B*, 1994, **50**, 17953–17979.

7   J. P. Perdew, K. Burke and M. Ernzerhof, *Phys. Rev. Lett.*, 1996, **77**, 3865–3868.

8   S. Grimme, *J. Comput. Chem.*, 2006, **27**, 1787–1799.

9   R. Dronskowski and P. E. Bloechl, *J. Phys. Chem.*, 1993, **97**, 8617–8624.

10   V. L. Deringer, A. L. Tchougréeff and R. Dronskowski, *J. Phys. Chem. A*, 2011, **115**, 5461–5466.

11   S. Maintz, V. L. Deringer, A. L. Tchougréeff and R. Dronskowski, *J. Comput. Chem.*, 2013, **34**, 2557–2567.

12   S. Maintz, V. L. Deringer, A. L. Tchougréeff and R. Dronskowski, *J. Comput. Chem.*, 2016, **37**, 1030–1035.

13   R. Nelson, C. Ertural, J. George, V. L. Deringer, G. Hautier and R. Dronskowski, *J. Comput. Chem.*, 2020, **41**, 1931–1940.

14   J. K. Nørskov, J. Rossmeisl, A. Logadottir, L. Lindqvist, J. R. Kitchin, T. Bligaard and H. Jónsson, *J. Phys. Chem. B*, 2004, **108**, 17886–17892.

15   Á. Valdés, Z. W. Qu, G. J. Kroes, J. Rossmeisl and J. K. Nørskov, *J. Phys. Chem. C*, 2008, **112**, 9872–9879.

16   A. A. Peterson, F. Abild-Pedersen, F. Studt, J. Rossmeisl and J. K. Nørskov, *Energy Environ. Sci.*, 2010, **3**, 1311–1315.

17   Z. Li, Z. Zhuang, F. Lv, H. Zhu, L. Zhou, M. Luo, J. Zhu, Z. Lang, S. Feng, W. Chen,

L. Mai and S. Guo, *Adv. Mater.*, 2018, **30**, 1803220.

18   K. Chen, K. Liu, P. An, H. Li, Y. Lin, J. Hu, C. Jia, J. Fu, H. Li, H. Liu, Z. Lin, W. Li, J. Li, Y. R. Lu, T. S. Chan, N. Zhang and M. Liu, *Nat. Commun.*, 2020, **11**, 1–8.

19   J. Zhang, Y. Zhao, C. Chen, Y.-C. Huang, C.-L. Dong, C.-J. Chen, R.-S. Liu, C. Wang, K. Yan, Y. Li and G. Wang, *J. Am. Chem. Soc.*, 2019, **141**, 20118–20126.

20   K. Yuan, D. Lützenkirchen-Hecht, L. Li, L. Shuai, Y. Li, R. Cao, M. Qiu, X. Zhuang, M. K. H. Leung, Y. Chen and U. Scherf, *J. Am. Chem. Soc.*, 2020, **142**, 2404–2412.

21   C. Hou, L. Zou, L. Sun, K. Zhang, Z. Liu, Y. Li, C. Li, R. Zou, J. Yu and Q. Xu, *Angew. Chemie*, 2020, **132**, 7454–7459.

22   S. H. Ahn, X. Yu and A. Manthiram, *Adv. Mater.*, 2017, **29**, 1606534.

23   P. Chen, T. Zhou, L. Xing, K. Xu, Y. Tong, H. Xie, L. Zhang, W. Yan, W. Chu, C. Wu and Y. Xie, *Angew. Chemie*, 2017, **129**, 625–629.

24   K. Strickland, E. Miner, Q. Jia, U. Tylus, N. Ramaswamy, W. Liang, M.-T. Sougrati, F. Jaouen and S. Mukerjee, *Nat. Commun.*, 2015, **6**, 7343.

25   Q. Liu, X. Liu, L. Zheng and J. Shui, *Angew. Chemie*, 2018, **130**, 1218–1222.

26   J.-D. Yi, R. Xu, Q. Wu, T. Zhang, K.-T. Zang, J. Luo, Y.-L. Liang, Y.-B. Huang and R. Cao, *ACS Energy Lett.*, 2018, **3**, 883–889.

27   Z. Zhang, J. Sun, F. Wang and L. Dai, *Angew. Chemie*, 2018, **130**, 9176–9181.

28   Q. Li, W. Chen, H. Xiao, Y. Gong, Z. Li, L. Zheng, X. Zheng, W. Yan, W. Cheong, R. Shen, N. Fu, L. Gu, Z. Zhuang, C. Chen, D. Wang, Q. Peng, J. Li and Y. Li, *Adv. Mater.*, 2018, **30**, 1800588.

29   Y. Chen, S. Ji, Y. Wang, J. Dong, W. Chen, Z. Li, R. Shen, L. Zheng, Z. Zhuang, D. Wang and Y. Li, *Angew. Chemie*, 2017, **129**, 7041–7045.

30   R. Jiang, L. Li, T. Sheng, G. Hu, Y. Chen and L. Wang, *J. Am. Chem. Soc.*, 2018, **140**, 11594–11598.

31   L. Jiao, G. Wan, R. Zhang, H. Zhou, S. Yu and H. Jiang, *Angew. Chemie Int. Ed.*, 2018, **57**, 8525–8529.

32   Z. Zhang, X. Gao, M. Dou, J. Ji and F. Wang, *Small*, 2017, **13**, 1604290.